J. Fluid Mech. (2023), *vol*. 954, R1, doi:10.1017/jfm.2022.1010

Latitudinal regionalization of rotating spherical shell convection

Thomas Gastine[1],† **and Jonathan M. Aurnou**[2]

[1]Université Paris Cité, Institut de Physique du Globe de Paris, UMR 7154 CNRS, 1 rue Jussieu, F-75005 Paris, France

[2]Department of Earth, Planetary, and Space Sciences, University of California, Los Angeles, CA 90095, USA

(Received 29 July 2022; revised 12 October 2022; accepted 28 November 2022)

Convection occurs ubiquitously on and in rotating geophysical and astrophysical bodies. Prior spherical shell studies have shown that the convection dynamics in polar regions can differ significantly from the lower latitude, equatorial dynamics. Yet most spherical shell convective scaling laws use globally-averaged quantities that erase latitudinal differences in the physics. Here we quantify those latitudinal differences by analysing spherical shell simulations in terms of their regionalized convective heat-transfer properties. This is done by measuring local Nusselt numbers in two specific, latitudinally separate, portions of the shell, the polar and the equatorial regions, Nu_p and Nu_e, respectively. In rotating spherical shells, convection first sets in outside the tangent cylinder such that equatorial heat transfer dominates at small and moderate supercriticalities. We show that the buoyancy forcing, parameterized by the Rayleigh number Ra, must exceed the critical equatorial forcing by a factor of $\approx$20 to trigger polar convection within the tangent cylinder. Once triggered, Nu_p increases with Ra much faster than does Nu_e. The equatorial and polar heat fluxes then tend to become comparable at sufficiently high Ra. Comparisons between the polar convection data and Cartesian numerical simulations reveal quantitative agreement between the two geometries in terms of heat transfer and averaged bulk temperature gradient. This agreement indicates that rotating spherical shell convection dynamics is accessible both through spherical simulations and via reduced investigatory pathways, be they theoretical, numerical or experimental.

Key words: Bénard convection, rotating flows, geostrophic turbulence

1. Introduction

It has long been known that rotating spherical shell convection significantly differs between the low latitudes (e.g. Busse & Cuong 1977; Gillet & Jones 2006) situated

† Email address for correspondence: gastine@ipgp.fr

outside the axially aligned cylinder that circumscribes the inner spherical shell boundary (the tangent cylinder, TC) and the higher latitude polar regions lying within the TC (e.g. Aurnou *et al.* 2003; Sreenivasan & Jones 2006; Aujogue *et al.* 2018; Cao, Yadav & Aurnou 2018). Further, in the atmosphere–ocean literature, latitudinal separation into polar, mid-latitude, extra-tropical and tropical zones is essential to accurately model the large-scale dynamics (e.g. Vallis 2017). Yet few scaling studies of spherical shell convection consider the innate regionalization of the dynamics (cf. Wang *et al.* 2021), and instead mostly focus on globally averaged quantities (e.g. Gastine, Wicht & Aubert 2016; Long *et al.* 2020).

In the turbulent rapidly rotating limit, theory requires the convective heat transport to be independent of the fluid diffusivities irregardless of system geometry. This yields (e.g. Julien *et al.* 2012*b*; Plumley & Julien 2019)

$$Nu \sim (Ra/Ra_c)^{3/2} \sim \widetilde{Ra}^{3/2} Pr^{-1/2} \sim Ra^{3/2} E^2 Pr^{-1/2}, \tag{1.1}$$

where, defined explicitly below, the Nusselt number Nu is the non-dimensional heat transfer, Ra (Ra_c) denotes the (critical) Rayleigh number, E is the Ekman number, Pr is the Prandtl number, and $\widetilde{Ra} \equiv Ra\, E^{4/3}$ expresses the generalized convective supercriticality (Julien *et al.* 2012*b*).

Cylindrical laboratory experiments with $Pr \approx 7$ and Cartesian (planar) numerical simulations with $Pr = (1, 7)$ and no-slip boundaries with $Ra/Ra_c \lesssim 10$ reveal a steep scaling $Nu \sim (Ra/Ra_c)^{\beta}$ with $\beta \approx 3$ (King, Stellmach & Aurnou 2012; Cheng *et al.* 2015, 2018). By comparing numerical models with stress-free and no-slip boundaries, Stellmach *et al.* (2014) showed that the steep $\beta \approx 3$ scaling is an Ekman pumping effect (cf. Julien *et al.* 2016). For larger supercriticalities, β decreases and gradually approaches (1.1). This $\beta \approx 3$ regime is expected to hold as long as the thermal boundary layers are in quasi-geostrophic balance, a condition approximated by $Ra\, E^{8/5} \lesssim 1$ (Julien *et al.* 2012*a*).

Globally averaged quantities in spherical shell models present several differences with the planar configuration. In particular, no steep $\beta \approx 3$ exponent is observed. Gastine *et al.* (2016) showed that the globally averaged heat transfer first follows a $Nu - 1 \sim Ra/Ra_c - 1$ weakly nonlinear scaling for $Ra \leq 6\, Ra_c$ before transitioning to a scaling close to (1.1) for $Ra > 6\, Ra_c$ and $RaE^{8/5} < 0.4$. Spherical shell models with a ratio between the inner radius r_i and the outer radius r_o of 0.35 and fixed-flux thermal conditions recover similar global scaling behaviours, though with a slightly larger exponent $\beta \approx 1.75$ for $E = 2 \times 10^{-6}$ (Long *et al.* 2020). Because the Ekman pumping enhancement of heat transfer is maximized when rotation and gravity are aligned, β is lower in the equatorial regions of spherical shells. This explains why globally averaged spherical β values cannot attain the $\beta \approx 3$ values found in planar (polar-like) studies.

Recently, Wang *et al.* (2021) analysed heat transfer within the equatorial regions, at mid-latitudes and inside the entire TC. They argued that the mid-latitude scaling in their models, similar to Gastine *et al.* (2016)'s global scaling, follows the diffusion-free scaling (1.1), while the region inside the TC follows a $\beta \approx 2.1$ trend. This TC-scaling exponent is significantly smaller than those obtained in planar models, possibly because of the finite inclination angle between gravity and the rotation axis averaged over the volume of the TC.

Following Wang *et al.* (2021), this study aims to better characterize the latitudinal variations in rotating convection dynamics and quantify the differences between spherical and non-spherical geometries. To do so, we carry out local heat transfer analyses in the polar and equatorial regions over an ensemble of $Pr = 1$ rotating spherical shell simulations with $r_i/r_o = 0.35$ and $r_i/r_o = 0.6$.

2. Hydrodynamical model

We consider a volume of fluid bounded by two spherical surfaces of inner radius r_i and outer radius r_o rotating about the z-axis with a constant rotation rate Ω. Both boundaries are mechanically no-slip and are held at constant temperatures $T_o = T(r_o)$ and $T_i = T(r_i)$. We adopt a dimensionless formulation of the Navier–Stokes equations using the shell gap $d = r_o - r_i$ as the reference length scale, the temperature contrast $\Delta T = T_o - T_i$ as the temperature unit, and the inverse of the rotation rate Ω^{-1} as the time scale. Under the Boussineq approximation, this yields the following set of dimensionless equations for the velocity $\boldsymbol{u}$ and temperature T expressed in spherical coordinates:

$$\frac{\partial \boldsymbol{u}}{\partial t} + \boldsymbol{u}\cdot\boldsymbol{\nabla}\boldsymbol{u} + 2\boldsymbol{e_z}\times\boldsymbol{u} = -\boldsymbol{\nabla}p + \frac{RaE^2}{Pr}T\,g(r)\boldsymbol{e_r} + E\,\nabla^2\boldsymbol{u}, \quad \boldsymbol{\nabla}\cdot\boldsymbol{u} = 0, \tag{2.1a,b}$$

$$\frac{\partial T}{\partial t} + \boldsymbol{u}\cdot\boldsymbol{\nabla}T = \frac{E}{Pr}\nabla^2 T, \tag{2.2}$$

where p corresponds to the non-hydrostatic pressure, g to gravity and $\boldsymbol{e_r}$ ($\boldsymbol{e_z}$) denotes the unit vector in the radial (axial) direction. The above equations are governed by the dimensionless Rayleigh, Ekman and Prandtl numbers, respectively defined by

$$Ra = \frac{\alpha g_o \Delta T d^3}{\nu\kappa}, \quad E = \frac{\nu}{\Omega d^2}, \quad Pr = \frac{\nu}{\kappa}, \tag{2.3a–c}$$

where ν and κ correspond to the constant kinematic viscosity and thermal diffusivity, g_o is the gravity at the external radius and α is the thermal expansion coefficient. Two spherical shell configurations are employed: (i) a thin shell with $r_i/r_o = 0.6$ under the assumption of a centrally condensed mass with $g = (r_o/r)^2$ (Gilman & Glatzmaier 1981); (ii) a self-gravitating thicker spherical shell model with $r_i/r_o = 0.35$ and $g = r/r_o$. The latter corresponds to the standard configuration employed in numerical models of Earth's dynamo (e.g. Christensen & Aubert 2006; Schwaiger, Gastine & Aubert 2019). We consider numerical simulations with $10^4 \leq Ra \leq 10^{11}$, $10^{-7} \leq E \leq 10^{-2}$ and $Pr = 1$ computed with the open source code MagIC (https://github.com/magic-sph/magic.) (Wicht 2002; Gastine & Wicht 2012). We mostly build the current study on existing numerical simulations from Gastine *et al.* (2016) and Schwaiger, Gastine & Aubert (2021) and continue their time integration to gather additional diagnostics when required.

In the following analyses overbars denote time averages, triangular brackets denote azimuthal averages and square brackets denote averages about the angular sectors comprised between the colatitudes $\theta_0 - \alpha$ and $\theta_0 + \alpha$ in radians:

$$\bar{f} = \int_{t_0}^{t_0+\tau} f\,\mathrm{d}t, \quad \langle f\rangle = \frac{1}{2\pi}\int_0^{2\pi} f(r,\theta,\phi,t)\,\mathrm{d}\phi, \quad [f]_{\theta_0}^{\alpha} = \frac{1}{\mathcal{S}_{\theta_0}^{\alpha}}\int_{\mathcal{S}_{\theta_0}^{\alpha}} f(r,\theta,\phi,t)\,\mathrm{d}\mathcal{S}, \tag{2.4a–c}$$

with $\mathrm{d}\mathcal{S} = \sin\theta\,\mathrm{d}\theta\mathrm{d}\theta$ and $\mathcal{S}_{\theta_0}^{\alpha} = \int_{\min(\theta_0-\alpha,0)}^{\max(\theta_0+\alpha,\pi)} \sin\theta\,\mathrm{d}\theta$.

For the sake of clarity, we introduce the following notations to characterize the time-averaged radial distribution of temperature:

$$\vartheta(r) = [\langle\bar{T}\rangle]_{\pi/2}^{\pi/2}, \quad \vartheta_e(r) = [\langle\bar{T}\rangle]_{\pi/2}^{\pi/36}, \quad \vartheta_p(r) = \frac{1}{2}\left([\langle\bar{T}\rangle]_0^{\pi/36} + [\langle\bar{T}\rangle]_{\pi}^{\pi/36}\right), \tag{2.5a–c}$$

where ϑ_e and ϑ_p correspond to the averaged radial distribution of temperature in the equatorial and polar regions, respectively, and $\alpha = \pi/36$ rad corresponds to 5° in

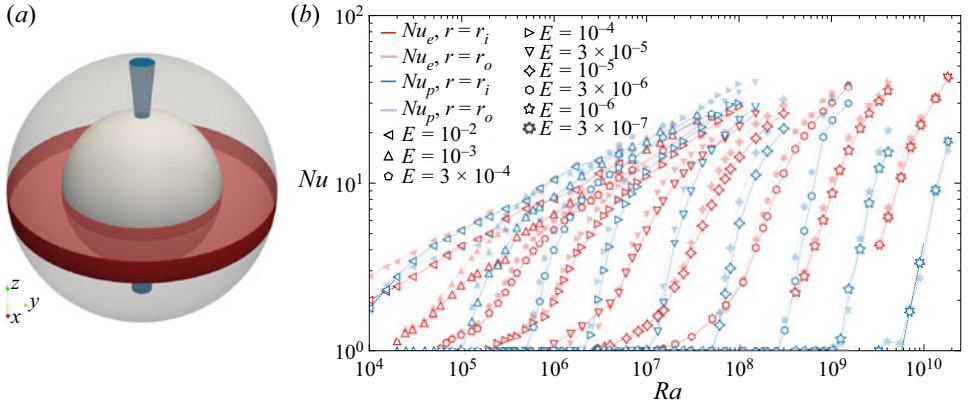

Figure 1. (*a*) Schematic showing the area selection to compute (2.7*a*,*b*), the local polar (blue) and equatorial (red) Nusselt numbers. (*b*) Time-averaged local Nusselt numbers in the polar (Nu_p) and equatorial (Nu_e) regions as a function of the Rayleigh number for spherical shell simulations with $r_i/r_o = 0.6$ and $g = (r_o/r)^2$ and $Pr = 1$ (Gastine *et al.* 2016). The different Ekman numbers are denoted by different symbol shapes, the two spherical shells surfaces r_i and r_o are marked by open and filled symbols, and by lower levels of opacity, respectively.

colatitudinal angle. The schematic shown in figure 1(*a*) highlights the fluid volumes involved in these measures. The value of $\alpha = 5^\circ$ is quite arbitrary and has been adopted to allow a comparison of polar data with local planar Rayleigh–Bénard convection (hereafter RBC) models while keeping a sufficient sampling.

To quantify the differences between the heat transfer in the polar and equatorial regions, we introduce a Nusselt number that depends on colatitude θ via

$$Nu_i(\theta) = \frac{\left.\dfrac{\mathrm{d}\langle\bar{T}\rangle}{\mathrm{d}r}\right|_{r_i}}{\left.\dfrac{\mathrm{d}T_c}{\mathrm{d}r}\right|_{r_i}}, \quad Nu_o(\theta) = \frac{\left.\dfrac{\mathrm{d}\langle\bar{T}\rangle}{\mathrm{d}r}\right|_{r_o}}{\left.\dfrac{\mathrm{d}T_c}{\mathrm{d}r}\right|_{r_o}}, \quad \frac{\mathrm{d}T_c}{\mathrm{d}r} = -\frac{r_i r_o}{r^2}, \tag{2.6a–c}$$

where T_c corresponds to the dimensionless temperature of the conducting state. The corresponding local Nusselt numbers in the equatorial and polar regions are then defined by

$$Nu_e = [Nu(\theta)]_{\pi/2}^{\pi/36}, \quad Nu_p = \frac{1}{2}\left([\langle Nu(\theta)\rangle]_0^{\pi/36} + [\langle Nu(\theta)\rangle]_\pi^{\pi/36}\right). \tag{2.7a,b}$$

We finally introduce the mid-shell time-averaged temperature gradient in the polar region:

$$\partial T = \frac{-\left.\dfrac{\mathrm{d}\vartheta_p}{\mathrm{d}r}\right|_{r=r_m}}{-\left.\dfrac{\mathrm{d}T_c}{\mathrm{d}r}\right|_{r=r_m}}, \quad r_m = \frac{1}{2}(r_i + r_o), \tag{2.8a,b}$$

where normalization by the conductive temperature gradient allows us to compare the scaling behaviour of ∂T between spherical shells of different radius ratio values, r_i/r_o, and planar models.

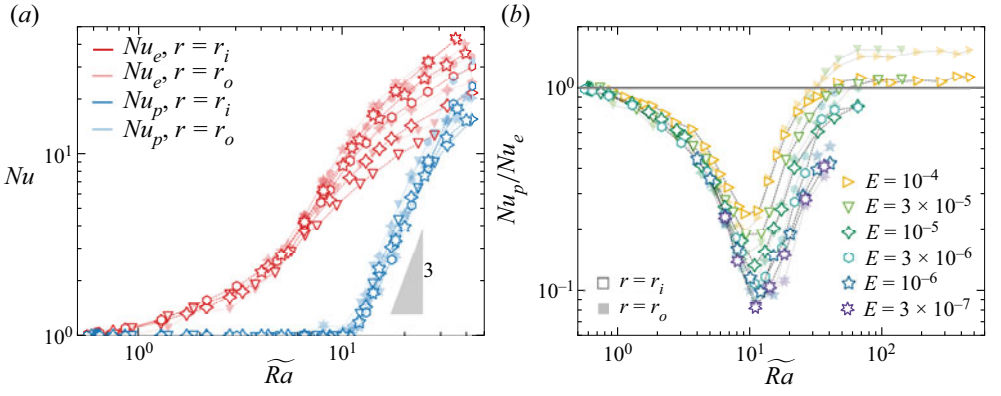

Figure 2. (*a*) Nusselt number in the polar (Nu_p) and in the equatorial (Nu_e) regions as a function of $\widetilde{Ra} = Ra\,E^{4/3}$ in the $r_i/r_o = 0.6$ simulations. The symbols carry the same meaning as in figure 1 but with only the $Ra\,E^{8/5} < 2$ simulations retained. (*b*) Ratio of polar and equatorial heat transfer Nu_p/Nu_e as a function of $\widetilde{Ra}$ for both spherical shell boundaries and $E \leq 10^{-4}$.

3. Results

Figure 1(*b*) shows Nu_p and Nu_e as a function of Ra for various E at both boundaries, r_i and r_o, for spherical shell simulations with $r_i/r_o = 0.6$ and $g = (r_o/r)^2$. Rotation delays the onset of convection such that the critical Rayleigh number required to trigger convective motions increases with decreasing Ekman number, $Ra_c \sim E^{-4/3}$. Convection first sets in outside the TC (e.g. Dormy *et al.* 2004). For each Ekman number, heat transfer behaviour in the equatorial regions (red symbols) first raises slowly following a weakly nonlinear scaling (e.g. Gillet & Jones 2006), before gradually rising in the vicinity of $Nu_e \approx 2$. At $Nu_e \gtrsim 2$, the heat transfer increases more steeply with Ra, before gradually tapering off toward the non-rotating RBC trend (e.g. Gastine, Wicht & Aurnou 2015). For $Ra/Ra_c > O(10)$, convection sets in in the polar regions and Nu_p steeply rises with Ra with a much larger exponent than Nu_e. At still larger forcings, the slope of Nu_p gradually decreases and comparable amplitudes in polar and equatorial heat transfers are observed. Heat-transfer scalings at both spherical shell boundaries r_i and r_o follow similar trends.

Figure 2 shows (*a*) Nu_p and Nu_e and (*b*) their ratio Nu_p/Nu_e plotted at both boundaries as a function of the supercriticality parameter $\widetilde{Ra} = RaE^{4/3}$. For $\widetilde{Ra} < 4$, Nu_e increases following the weakly nonlinear form $Nu_e - 1 \sim Ra/Ra_c - 1$ (Gastine *et al.* 2016, § 3.1). For larger supercriticalities, the Nu_e scaling steepens and an additional E-dependence causes the data to fan out, possibly because these highest $\widetilde{Ra}$ cases do not fulfil $Ra\,E^{8/5} < 0.4$. There is no clear power-law scaling in the $Nu_e(\widetilde{Ra} < 10)$ data, but the steepest local slope yields $\max(\beta) \approx 1.9$ in the $5 \leq \widetilde{Ra} \leq 10$ range.

Best fits to the figure 2(*a*) data show that polar convection onsets at $\widetilde{Ra}(E) = 11.2 \pm 0.3$ in the $r_i/r_o = 0.6$ simulations. The mean value of the critical polar Rayleigh number is

$$Ra_c^p = 11.2\,E^{-4/3}. \tag{3.1}$$

Although the polar onset of convection, estimated via $Ra_c^p\,E^{4/3}$, remains nearly constant, the global (e.g. low latitude) onset value, estimated by $Ra_c\,E^{4/3}$, varies by a factor of ≈2 over our E range. Their ratio then yields

$$Ra_c^p(E)/Ra_c(E) = 20 \pm 5. \tag{3.2}$$

This means that rotating convection does not typically onset in the polar regions until the lower latitude convection is already 20 times supercritical and is already operating under highly supercritical conditions. This difference in equator vs polar convective onsets imparts a significant regionalization to rotating spherical shell convection right from the get go.

We find, throughout this investigation, that polar rotating convection compares closely to its plane-layer counterpart. However, it is not expected that the polar critical Rayleigh number will exactly agree with plane-layer predictions, due to the effects of finite spherical curvature as well as the radial variations of gravity in these $r_i/r_o = 0.6$ simulations. In the rapidly rotating thin-shell limit, in which $r_i/r_o \to 1$ and E is kept asymptotically small, Ra_c^p will likely approach the planar value. Still, the polar scaling in (3.1) is found to be 51 % of the plane-layer $E \to 0$ scaling prediction, $Ra_c = 21.9\,E^{-4/3}$ (Kunnen 2021), and to be 56 % of Niiler & Bisshopp (1965)'s finite Ekman number, no-slip plane layer Ra_c prediction at $E = 10^{-6}$. In addition to the similarity in critical Ra values, it is found that the polar heat transfer Nu_p rises sharply once polar convection onsets, following a $Nu_p \sim \widetilde{Ra}^3$ scaling that matches the heat-transfer scalings found in no-slip planar simulations carried out over the same (E, Pr) ranges (King *et al.* 2012; Stellmach *et al.* 2014; Aurnou *et al.* 2015).

Figure 2(*b*) shows the ratio of polar to equatorial heat transport, which follows a distinct V-shape trend that can be decomposed in three regions: (i) for $\widetilde{Ra} < 11.2$, $Nu_p \approx 1$ and the ratio depends directly on $Nu_e = f(\widetilde{Ra})$; (ii) for $11.2 < \widetilde{Ra} \lesssim 30$, Nu_p raises much faster than Nu_e hence increasing Nu_p/Nu_e; (iii) when rotational effects become less influential, $Nu_p/Nu_e \approx 1$ at r_i and $Nu_p/Nu_e \approx 1.5$ at r_o.

Figure 3(*a*,*b*) shows the time-averaged temperature profiles in the polar and equatorial regions (ϑ_p dashed lines and ϑ_e dot-dashed lines) alongside the volume-averaged temperature (ϑ, solid line) for two numerical models with $r_i/r_o = 0.6$, $g = (r_o/r)^2$, $E = 10^{-6}$ and different Ra. For the case with $Ra \approx 14.1\,Ra_c$ (figure 3*a*), low-latitude convection is active but has yet to start within the TC. The mean temperature in the polar regions ϑ_p thus closely follows the conductive profile T_c (dotted line), while in the equatorial region we observe the formation of a thin thermal boundary layer at r_i and a decrease of the temperature gradient in the fluid bulk. At larger convective forcing ($Ra \approx 69.3\,Ra_c$, figure 3*b*), convection is space-filling. The temperature profiles in the polar and equatorial regions become comparable and a larger fraction of the temperature contrast is accommodated in the thermal boundary layers.

Figure 3(*c*) shows the latitudinal variations of the heat flux at both spherical shell boundaries for increasing supercriticalities. These profiles confirm that convection first sets in outside the TC while the high-latitude regions remain close to the conductive $Nu = 1$ state up to Ra_c^p, and that the $Ra > Ra_c^p$ polar transfer rises quickly, thus reducing the latitudinal Nu contrast. Both spherical-shell boundaries feature similar global trends, with interesting regionalized differences. The TC (solid vertical lines) is visible, for instance, in the outer-boundary heat transfer $Nu_o(\theta)$, manifesting itself in local maxima that persist between $15\,Ra_c$ and $70\,Ra_c$.

Figure 4 shows (*a*) Nu_p and (*b*) normalized mid-depth polar temperature gradients ∂T as a function of Ra/Ra_c^p for spherical-shell simulations with $r_i/r_o = 0.6$ and $r_i/r_o = 0.35$, and for Cartesian asymptotically reduced models (e.g. Plumley *et al.* 2016) and $E \geq 2 \times 10^{-7}$, $Pr = 1$ direct numerical simulations (Stellmach *et al.* 2014). In this figure, Ra_c^p is used for the critical Ra values for spherical-shell data, whereas standard planar Ra_c values are used for the plane-layer data. Good quantitative agreement is found in the Nu_p and ∂T

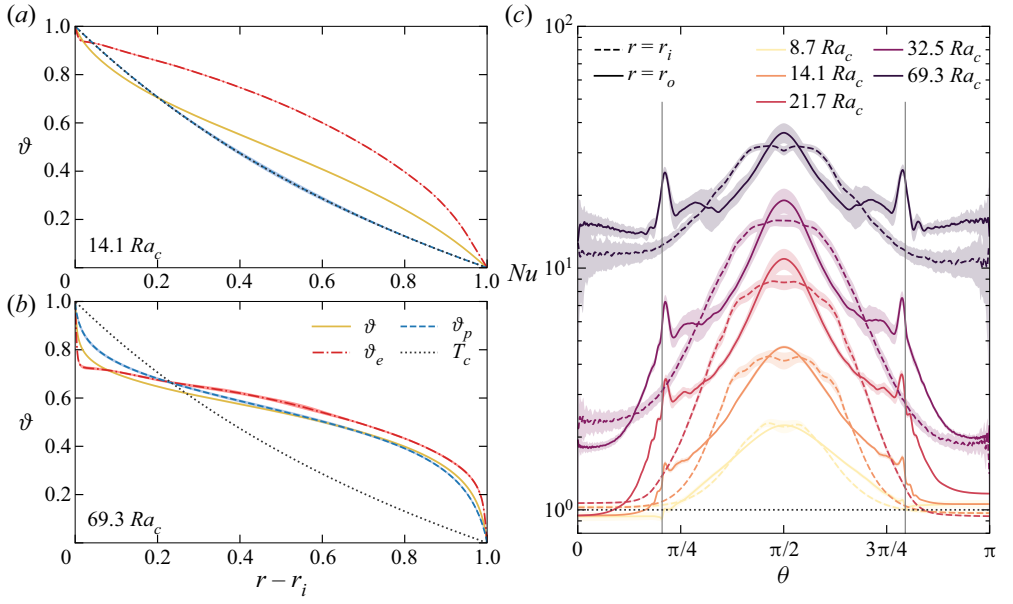

Figure 3. (*a*,*b*) Radial profiles of time-averaged temperature in the polar regions (blue dashed line), in the equatorial region (red dot-dashed line) and averaged of the entire spherical surface (tan solid line). For comparison, the conducting temperature profile T_c is also plotted as a black dotted line. Panel (*a*) corresponds to $r_i/r_o = 0.6$, $g = (r_o/r)^2$, $E = 10^{-6}$, $Ra = 6.5 \times 10^8$, $Pr = 1$, while (*b*) corresponds to $r_i/r_o = 0.6$, $g = (r_o/r)^2$, $E = 10^{-6}$, $Ra = 3.2 \times 10^9$ and $Pr = 1$. (*c*) Time-averaged local Nusselt number at both spherical shell boundaries as a function of the colatitude for simulations with $r_i/r_o = 0.6$, $g = (r_o/r)^2$, $E = 10^{-6}$, $Pr = 1$ and increasing supercriticalities. Solid (dashed) lines correspond to r_i (r_o). The vertical solid lines mark the location of the TC. In all panels, the shaded regions correspond to one standard deviation about the time averages.

data from spherical shell and planar models, with all the data sets effectively overlying one another. The $1 \lesssim Ra/Ra_c^p \lesssim 3$ heat transfer follows a $Nu_p \sim (Ra/Ra_c)^3$ scaling in all the data sets. At larger supercriticalities, the scaling exponent of Nu_p decreases and the asymptotic $\beta = 3/2$ scaling appears to be approached in the highest supercriticality planar cases. The mid-depth temperature gradients quantitatively agree in all models as well, attaining a relatively large minimum value, $\partial T \approx 0.5$ near $Ra \approx 3\,Ra_c^p$, before increasing slightly in the highest supercriticality planar models.

4. Discussion

Globally averaged heat-transfer scalings for rotating convection differ between spherical and planar geometries with the latter yielding steeper *Nu*-*Ra* scaling trends. By introducing regionalized measures of heat transfer, we have shown that this steep scaling can also be recovered in the polar regions of spherical shells. The comparisons in figure 4 reveal an almost perfect overlap in heat-transfer data between the two geometries. Importantly, this demonstrates that local, non-spherical models can be used to understand spherical systems (e.g. Julien *et al.* 2012*b*; Horn & Shishkina 2015; Cabanes *et al.* 2017; Calkins 2018; Cheng *et al.* 2018; Miquel *et al.* 2018; Gastine 2019).

Our regional analysis shows that the use of global volume-averaged properties to interpret rotating spherical shell convection can be misleading since such averages are often made over regions with significantly differing convection dynamics (e.g. Ecke & Niemela 2014; Lu *et al.* 2021; Grannan *et al.* 2022, in rotating cylinders). As such, it is

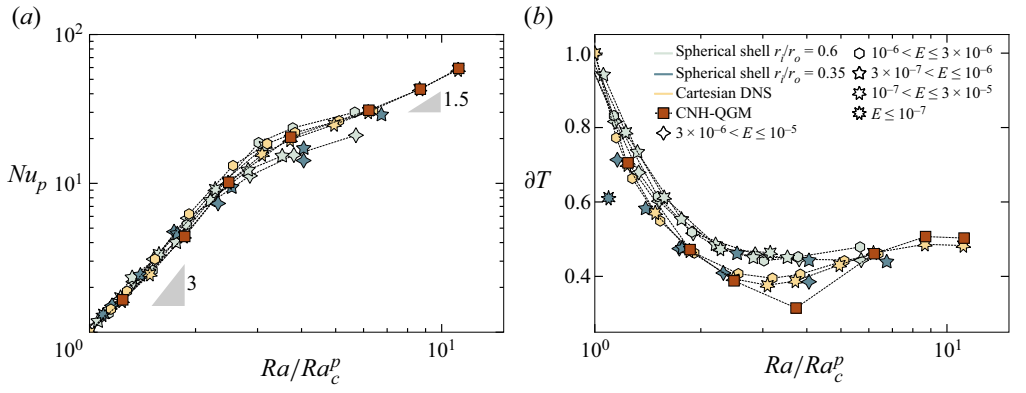

Figure 4. (*a*) Nusselt number in the polar regions Nu_p as a function of the local supercriticality Ra/Ra_c^p. (*b*) Normalized mid-depth temperature gradient (2.8*a*,*b*) in the polar regions ∂T as a function of the local supercriticality. Spherical-shell simulations include two configurations with $r_i/r_o = 0.6$ and $g = (r_o/r)^2$ (light blue symbols, from Gastine *et al.* 2016) and $r_i/r_o = 0.35$ and $g = r/r_o$ (dark blue symbols, from Schwaiger *et al.* 2021). All the simulations with $E \leq 10^{-5}$ and $Nu_p > 1$ have been retained. Direct numerical simulations (DNS) in Cartesian geometry with periodic horizontal boundary conditions (light yellow symbols) come from Stellmach *et al.* (2014), while non-hydrostatic quasi-geostrophic models (CNH-QGM) (red symbols) come from Plumley *et al.* (2016).

quite likely that globally averaged β depends on the spherical shell radius ratio, r_i/r_o. In higher r_i/r_o shells, more of the fluid will lie within the TC and the globally averaged β will tend towards a polar value near 3. In contrast, lower r_i/r_o shells should trend towards regional β values below 2, as found in our Nu_e data. We hypothesize further that the mid-latitude $\beta \simeq 3/2$ scaling in (Wang *et al.* 2021) may represent a combination of the low- and high-latitude scalings, which could also be tested by varying r_i/r_o.

A similar argument may also explain Wang *et al.* (2021)'s higher latitude, TC heat-transfer scaling of $\beta = 2.1$. We postulate that measuring the rotating heat transfer away from the poles will always yield $\beta < 3$. This may be further exacerbated if the heat transfer is measured across the TC, which likely acts as a radial transport barrier (e.g. Guervilly & Cardin 2017; Cao *et al.* 2018). Thus, Wang *et al.* (2021)'s $\beta \approx 2.1$ value may arise because their whole TC measurements extend to far lower latitudes in comparison with the far tighter, pole-adjacent Nu_p measurements made here that yield $\beta \approx 3$.

The polar heat-transfer data in figure 2 demonstrates a sharp convective onset value, with $Ra_c^p = (11.2 \pm 0.3)E^{-4/3}$ over our range of $r_i/r_o = 0.6$ models and $Ra_c^p/Ra_c = 20 \pm 5$. It is likely that convective turbulence is space-filling in planetary fluid layers. We argue then that realistic geophysical and astrophysical models of rotating convection require $Ra > Ra_c^p$. If the convection is rapidly rotating as well, this constrains the convective Rossby number $Ro_{conv} = (RaE^2/Pr)^{1/2} \lesssim 0.1$ (e.g. Christensen & Aubert 2006; Aurnou, Horn & Julien 2020). Thus, space-filling rotating convective turbulence simultaneously requires $Ra \gtrsim 10Ra_c^p$ and $Ro_{conv} \lesssim 1/10$, which then constrains that $E \lesssim 10^{-6}$ in $Pr \simeq 1$ models. Such dynamical constraints are important for building accurate models of $Nu(\theta)$, which are essential to our interpretations of planetary and astrophysical observations. For instance, on the icy satellites, latitudinal changes in ice shell thickness and surface terrain likely reflect the latitudinally varying convective dynamics in the underlying oceans (e.g. Soderlund *et al.* 2020). We hypothesize that the broad array of Nu_p/Nu_e solutions found in the models (e.g. Soderlund 2019; Amit *et al.* 2020; Bire *et al.* 2022) could possibly arise

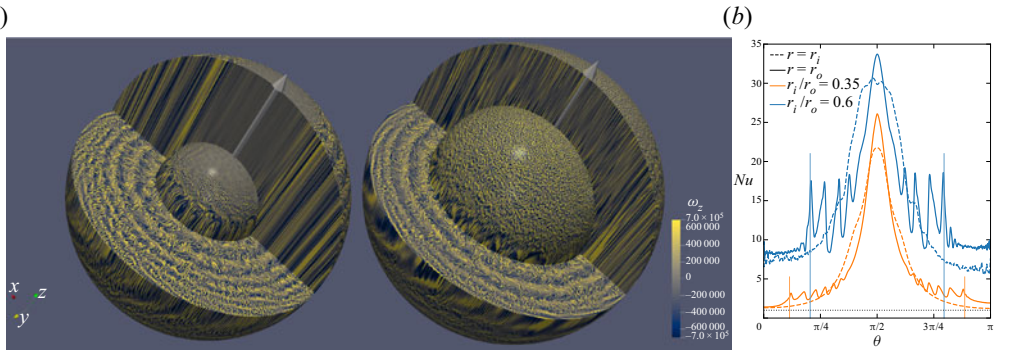

Figure 5. (*a*,*b*) Meridional sections, equatorial cut and radial surfaces of the axial component of the vorticity $\omega_z = \boldsymbol{e_z} \cdot \boldsymbol{\nabla} \times \boldsymbol{u}$. Panel (*a*) corresponds to a numerical model with $r_i/r_o = 0.35$, $g = r/r_o$, $E = 10^{-7}$, $Ra = 10^{11}$ and $Pr = 1$, while (*b*) corresponds to a numerical model with $r_i/r_o = 0.6$, $g = (r_o/r)^2$, $E = 3 \times 10^{-7}$, $Ra = 1.3 \times 10^{10}$ and $Pr = 1$. (*c*) Local Nusselt number at both spherical-shell boundaries as a function of the colatitude. The orange and blue lines correspond to the numerical model shown in (*a*,*b*), respectively. The location of the TC for both radius ratios is marked by vertical solid lines.

because convection is not active within the TC in some of the models, and is not rapidly rotating in others. Our results suggest that quantitative comparisons in heat-flux profiles can only be made between models having similar latitudinal distributions of convective activity and comparable Rossby number values.

Establishing asymptotically accurate trends for Nu_p/Nu_e also requires accurate scaling laws for the equatorial heat transfer. A brief inspection of figure 2 reveals the complexity of $Nu_e(\widetilde{Ra})$, and its lack of any clear power-law trend. To further complicate this task, zonal jets tend to develop in no-slip cases with $E \lesssim 10^{-6}$, which can substantively alter the patterns of convective heat flow. Figure 5(*a*,*b*) shows axial vorticity $\omega_z = \boldsymbol{e_z} \cdot \boldsymbol{\nabla} \times \boldsymbol{u}$ snapshots and figure 5(*c*) latitudinal heat-flux profiles for two $E < 10^{-6}$ simulations with different radius ratios. Convection in the figure 5(*a*) $r_i/r_o = 0.35$ case is sub-critical inside the TC, while it is space-filling in the figure 5(*b*) $r_i/r_o = 0.6$ simulation. In the latter case, polar convection develops as small-scale axially aligned vortices which do not drive jets within the TC. In contrast, the convective motions outside the TC are already sufficiently turbulent in both cases to trigger the formation of zonal jets. These jet flows manifest via the formation of alternating, concentric rings of positive and negative axial vorticity. These coherent zonal motions act to reduce the heat-transfer efficiency in the regions of intense shear where the zonal velocities become of comparable amplitude to the convective flow (e.g. Aurnou *et al.* 2008; Yadav *et al.* 2016; Guervilly & Cardin 2017; Raynaud *et al.* 2018; Soderlund 2019). Thus, the outer-boundary heat-flux profile $Nu_o(\theta)$ in figure 5(*c*) adopts a strongly undulatory structure exterior to the TC. The asymptotic scaling behaviour of Nu_e is hence intimately related to the spatial distribution and amplitude of the zonal jets that develop in the shell, a topic for future investigations of rotating convective turbulence (e.g. Lonner, Aggarwal & Aurnou 2022).

Acknowledgements. We thank S. Stellmach and K. Julien for sharing their planar convection data and the reviewers for their constructive comments that improved upon the final manuscript. We also thank the University of Leiden's Lorentz Center, where this study was resuscitated during the 'Rotating Convection: from the Lab to the Stars' workshop.

Funding. Simulations requiring longer time integrations to gather diagnostics were computed on GENCI (Grant 2021-A0070410095) and on the S-CAPAD platform at IPGP. JMA gratefully acknowledges the support of the NSF Geophysics Program (EAR 2143939).

Declaration of interests. The authors report no conflict of interest.

Author ORCIDs.
Thomas Gastine https://orcid.org/0000-0003-4438-7203;
Jonathan M. Aurnou https://orcid.org/0000-0002-8642-2962.

References

Amit, H., Choblet, G., Tobie, G., Terra-Nova, F., Čadek, O. & Bouffard, M. 2020 Cooling patterns in rotating thin spherical shells – application to Titan's subsurface ocean. *Icarus* **338**, 113509.

Aujogue, K., Pothérat, A., Sreenivasan, B. & Debray, F. 2018 Experimental study of the convection in a rotating tangent cylinder. *J. Fluid Mech.* **843**, 355–381.

Aurnou, J., Andreadis, S., Zhu, L. & Olson, P. 2003 Experiments on convection in Earth's core tangent cylinder. *Earth Planet. Sci. Lett.* **212** (1–2), 119–134.

Aurnou, J.M., Heimpel, M.H., Allen, L.A., King, E.M. & Wicht, J. 2008 Convective heat transfer and the pattern of thermal emission on the gas giants. *Geophys. J. Intl* **173** (3), 793–801.

Aurnou, J.M., Horn, S. & Julien, K. 2020 Connections between nonrotating, slowly rotating, and rapidly rotating turbulent convection transport scalings. *Phys. Rev. Res.* **2** (4), 043115.

Aurnou, J.M., Calkins, M.A., Cheng, J.S., Julien, K., King, E.M., Nieves, D., Soderlund, K.M. & Stellmach, S. 2015 Rotating convective turbulence in Earth and planetary cores. *Phys. Earth Planet. Inter.* **246**, 52–71.

Bire, S., Kang, W., Ramadhan, A., Campin, J.-M. & Marshall, J. 2022 Exploring ocean circulation on icy moons heated from below. *J. Geophys. Res.* **127** (3), e07025.

Busse, F.H. & Cuong, P.G. 1977 Convection in rapidly rotating spherical fluid shells. *Geophys. Astrophys. Fluid Dyn.* **8** (1), 17–41.

Cabanes, S., Aurnou, J.M., Favier, B. & Le Bars, M. 2017 A laboratory model for deep-seated jets on the gas giants. *Nat. Phys.* **13** (4), 387–390.

Calkins, M.A. 2018 Quasi-geostrophic dynamo theory. *Phys. Earth Planet. Inter.* **276**, 182–189.

Cao, H., Yadav, R.K. & Aurnou, J.M. 2018 Geomagnetic polar minima do not arise from steady meridional circulation. *Proc. Natl Acad. Sci. USA* **115** (44), 11186–11191.

Cheng, J.S., Aurnou, J.M., Julien, K. & Kunnen, R.P.J. 2018 A heuristic framework for next-generation models of geostrophic convective turbulence. *Geophys. Astrophys. Fluid Dyn.* **112** (4), 277–300.

Cheng, J.S., Stellmach, S., Ribeiro, A., Grannan, A., King, E.M. & Aurnou, J.M. 2015 Laboratory-numerical models of rapidly rotating convection in planetary cores. *Geophys. J. Intl* **201**, 1–17.

Christensen, U.R. & Aubert, J. 2006 Scaling properties of convection-driven dynamos in rotating spherical shells and application to planetary magnetic fields. *Geophys. J. Intl* **166**, 97–114.

Dormy, E., Soward, A.M., Jones, C.A., Jault, D. & Cardin, P. 2004 The onset of thermal convection in rotating spherical shells. *J. Fluid Mech.* **501**, 43–70.

Ecke, R.E. & Niemela, J.J. 2014 Heat transport in the geostrophic regime of rotating Rayleigh–Bénard convection. *Phys. Rev. Lett.* **113** (11), 114301.

Gastine, T. 2019 pizza: an open-source pseudo-spectral code for spherical quasi-geostrophic convection. *Geophys. J. Intl* **217** (3), 1558–1576.

Gastine, T. & Wicht, J. 2012 Effects of compressibility on driving zonal flow in gas giants. *Icarus* **219**, 428–442.

Gastine, T., Wicht, J. & Aubert, J. 2016 Scaling regimes in spherical shell rotating convection. *J. Fluid Mech.* **808**, 690–732.

Gastine, T., Wicht, J. & Aurnou, J.M. 2015 Turbulent Rayleigh–Bénard convection in spherical shells. *J. Fluid Mech.* **778**, 721–764.

Gillet, N. & Jones, C.A. 2006 The quasi-geostrophic model for rapidly rotating spherical convection outside the tangent cylinder. *J. Fluid Mech.* **554**, 343–369.

Gilman, P.A. & Glatzmaier, G.A. 1981 Compressible convection in a rotating spherical shell. I – anelastic equations. *Astrophys. J. Suppl.* **45**, 335–349.

Grannan, A.M., Cheng, J.S., Aggarwal, A., Hawkins, E.K., Xu, Y., Horn, S., Sánchez-Álvarez, J. & Aurnou, J.M. 2022 Experimental pub crawl from Rayleigh–Bénard to magnetostrophic convection. *J. Fluid Mech.* **939**, R1.

Guervilly, C. & Cardin, P. 2017 Multiple zonal jets and convective heat transport barriers in a quasi-geostrophic model of planetary cores. *Geophys. J. Intl* **211** (1), 455–471.

HORN, S. & SHISHKINA, O. 2015 Toroidal and poloidal energy in rotating Rayleigh–Bénard convection. *J. Fluid Mech.* **762**, 232–255.

JULIEN, K., AURNOU, J.M., CALKINS, M.A., KNOBLOCH, E., MARTI, P., STELLMACH, S. & VASIL, G.M. 2016 A nonlinear model for rotationally constrained convection with Ekman pumping. *J. Fluid Mech.* **798**, 50–87.

JULIEN, K., KNOBLOCH, E., RUBIO, A.M. & VASIL, G.M. 2012*a* Heat transport in low-Rossby-number Rayleigh–Bénard convection. *Phys. Rev. Lett.* **109** (25), 254503.

JULIEN, K., RUBIO, A.M., GROOMS, I. & KNOBLOCH, E. 2012*b* Statistical and physical balances in low Rossby number Rayleigh–Bénard convection. *Geophys. Astrophys. Fluid Dyn.* **106**, 392–428.

KING, E.M., STELLMACH, S. & AURNOU, J.M. 2012 Heat transfer by rapidly rotating Rayleigh–Bénard convection. *J. Fluid Mech.* **691**, 568–582.

KUNNEN, R.P.J. 2021 The geostrophic regime of rapidly rotating turbulent convection. *J. Turbul.* **22** (4–5), 267–296.

LONG, R.S., MOUND, J.E., DAVIES, C.J. & TOBIAS, S.M. 2020 Scaling behaviour in spherical shell rotating convection with fixed-flux thermal boundary conditions. *J. Fluid Mech.* **889**, A7.

LONNER, T.L., AGGARWAL, A. & AURNOU, J.M. 2022 Planetary core-style rotating convective flows in paraboloidal laboratory experiments. *J. Geophys. Res.* **127** (10), e2022JE007356.

LU, H.-Y., DING, G.-Y., SHI, J.-Q., XIA, K.-Q. & ZHONG, J.-Q. 2021 Heat-transport scaling and transition in geostrophic rotating convection with varying aspect ratio. *Phys. Rev. Fluids* **6** (7), L071501.

MIQUEL, B., XIE, J.-H., FEATHERSTONE, N., JULIEN, K. & KNOBLOCH, E. 2018 Equatorially trapped convection in a rapidly rotating shallow shell. *Phys. Rev. Fluids* **3** (5), 053801.

NIILER, P.P. & BISSHOPP, F.E. 1965 On the influence of Coriolis force on onset of thermal convection. *J. Fluid Mech.* **22** (4), 753–761.

PLUMLEY, M. & JULIEN, K. 2019 Scaling laws in Rayleigh–Bénard convection. *Earth Space Sci.* **6** (9), 1580–1592.

PLUMLEY, M., JULIEN, K., MARTI, P. & STELLMACH, S. 2016 The effects of Ekman pumping on quasi-geostrophic Rayleigh–Bénard convection. *J. Fluid Mech.* **803**, 51–71.

RAYNAUD, R., RIEUTORD, M., PETITDEMANGE, L., GASTINE, T. & PUTIGNY, B. 2018 Gravity darkening in late-type stars. I. The Coriolis effect. *Astron. Astrophys.* **609**, A124.

SCHWAIGER, T., GASTINE, T. & AUBERT, J. 2019 Force balance in numerical geodynamo simulations: a systematic study. *Geophys. J. Intl* **219**, S101–S114.

SCHWAIGER, T., GASTINE, T. & AUBERT, J. 2021 Relating force balances and flow length scales in geodynamo simulations. *Geophys. J. Intl* **224** (3), 1890–1904.

SODERLUND, K.M. 2019 Ocean dynamics of outer solar system satellites. *Geophys. Res. Lett.* **46** (15), 8700–8710.

SODERLUND, K.M., *et al.* 2020 Ice-ocean exchange processes in the Jovian and Saturnian satellites. *Space Sci. Res.* **216** (5), 80.

SREENIVASAN, B. & JONES, C.A. 2006 Azimuthal winds, convection and dynamo action in the polar regions of planetary cores. *Geophys. Astrophys. Fluid Dyn.* **100** (4), 319–339.

STELLMACH, S., LISCHPER, M., JULIEN, K., VASIL, G., CHENG, J.S., RIBEIRO, A., KING, E.M. & AURNOU, J.M. 2014 Approaching the asymptotic regime of rapidly rotating convection: boundary layers versus interior dynamics. *Phys. Rev. Lett.* **113** (25), 254501.

VALLIS, G.K. 2017 *Atmospheric and Oceanic Fluid Dynamics*. Cambridge University Press.

WANG, G., SANTELLI, L., LOHSE, D., VERZICCO, R. & STEVENS, R.J.A.M. 2021 Diffusion-free scaling in rotating spherical Rayleigh–Bénard convection. *Geophys. Res. Lett.* **48** (20), e95017.

WICHT, J. 2002 Inner-core conductivity in numerical dynamo simulations. *Phys. Earth Planet. Inter.* **132**, 281–302.

YADAV, R.K., GASTINE, T., CHRISTENSEN, U.R., DUARTE, L.D.V. & REINERS, A. 2016 Effect of shear and magnetic field on the heat-transfer efficiency of convection in rotating spherical shells. *Geophys. J. Intl* **204**, 1120–1133.